

## COMPUTATIONAL FLUID DYNAMICS – A.A. 2024-2025

# Numerical Investigation of Aerodynamic Performance of a Formula 1 Rear Wing: DRS Activation and Gurney Flap

Francesco Lo Sardo, 231971

Gino Martella, 242619

Giorgio Pacchione, 252339

Davide Ruocchio, 216456

Luca Servadio, 245790

**Group number 19**

**Lecturers:**

Dr. Barbara Re

Dr. Andrea Rausa

## 1. Problem statement

In Formula 1 (F1), rear wings are one of the most impactful components on the aerodynamic performance of the car. Over the years, many strategies have been adopted to improve the design of the rear wings of Formula 1 cars. Among the most interesting ones are the Drag Reduction System and the Gurney flap.

The Drag Reduction System (DRS) was introduced as an active aerodynamic solution to address the persistent challenges associated with overtaking. First implemented in 2011, the DRS significantly alters the aerodynamic configuration of a car by reducing the angle of the rear wing flap, leading to a substantial drop in drag and allowing higher top speeds. The operation of the DRS is strictly regulated to maintain fairness in competition. It can only be activated in designated zones on the circuit, typically the longest straights, and is conditional upon the chasing car being within one second of the car ahead.

The Gurney flap (GF) is a small perpendicular appendage mounted on the pressure side of a wing at its trailing edge. It serves to significantly improve aerodynamic performance by increasing the lift or downforce of the wing, often with only a moderate increase in drag.

This paper presents a two-dimensional CFD analysis performed with the open-source software SU2. The pur of this work is to understand and reproduce the aerodynamics of such solutions while critically assessing the limitations and constraints of this approach.

The study focuses on a DRS setup and investigates the effects of unsteady and transient phenomena that may arise upon its activation. The Gurney flap is tested to evaluate its functioning and effectiveness limitedly to steady conditions.

## 2. Simulation Setup

### 2.1. Geometry

The rear wing used in this work is a two-element wing, with a mainplane and a DRS flap. Both are S1223 airfoils, of different chord. Each F1 team develops its own airfoil independently, and detailed information on the characteristics of these airfoils is not available. The S1223 airfoil is reported in a number of publications on this topic, and it has seen widespread use in minor series and student competitions.

The DRS chord is 60% with respect to that of the mainplane which was chosen equal to 1 m and acts as the reference unit for any measurements given hereinafter. The pitch angle of the moving flap is  $-40^\circ$  with respect to the horizontal axis.

The sliding mesh approach has been followed to allow for the rotation of the DRS flap only. It requires a portion of the domain, enclosing the DRS profile, to rotate without intersecting the mainplane. The rotating portion is a circle of radius  $r = 0.831$ , centered on the DRS hinge (at 80% of its chord), to ensure that the airfoil and its boundary layer mesh (of thickness 0.01) are fully enclosed. The use of a sliding mesh requires that the DRS is translated backward and upward with respect to its original location, resulting in a gap between its leading edge and the trailing edge of the mainplane equal to 0.007 along the  $x$ -direction and 0.049 along the  $y$ -direction.

The Gurney flap is modeled as a rectangular appendage attached to the trailing edge, perpendicular to the pressure side of the DRS wing. Two configurations have been tested, with heights equal to 0.01 and 0.02. In both cases, the thickness is 0.0026, as small changes in thickness are not expected to produce relevant effects [9]. These values agree with sources in the literature [2, 6], suggesting that heights above 2% of the reference chord may be detrimental to the performance of the wing.

**Sliding mesh approach** The only moving part in a DRS mechanism is the movable flap. To simulate this actuation, a rigid motion is imposed on a portion of the domain that includes the DRS flap, while the rest of the domain remains still. Different approaches have been developed in CFD environments to treat similar configurations, among which are overset grids and sliding meshes. Overset grids are not yet implemented in the latest version of SU2, while sliding meshes have been introduced starting from 2017, therefore, they have been employed for the purposes of this project.

In a sliding mesh approach the domain is divided into distinct zones that throughout the motion slide one against the other without overlapping. The portion of the mesh integral to the DRS flap fits in a hole carved out in the domain. The motion of the DRS flap is a rigid rotation; hence, the shape of such a hole must be circular to attain rotational symmetry. This is a non-trivial constraint, since the two airfoils are separated by a small gap. This translates into a geometric limitation on the location of the hinge and the relative positions of the two airfoils, and it also impacts the mesh topology.

The interface between the zones is critical to perform a trustworthy simulation. Here, elements on the two sides communicate through an interpolation algorithm, as discussed in Section 2.3.4. It is not required to have perfectly aligned cells at the interface, but it is desirable to have cells of similar sizes. This is achieved by refining a portion of the interface as detailed in Section 2.2.

The SU2 solver admits *multizone* meshes, eventually with individual configuration files attached to each zone. The parameters required for the moving mesh are specified in these configuration files. In the sliding mesh approach, to allow the exchange of information between the two zones, SU2 requires that a fictitious null rotation rate is imposed on the stationary zone of the mainplane as well.

## 2.2. Mesh generation

The mesh was generated with an O-grid approach. This topology adapts well to the restrictions imposed by the sliding mesh implementation, as it allows to generate a boundary layer mesh that does not intersect the moving interface. The center of the far-field circle is located in correspondence with the hinge about which the DRS rotates.

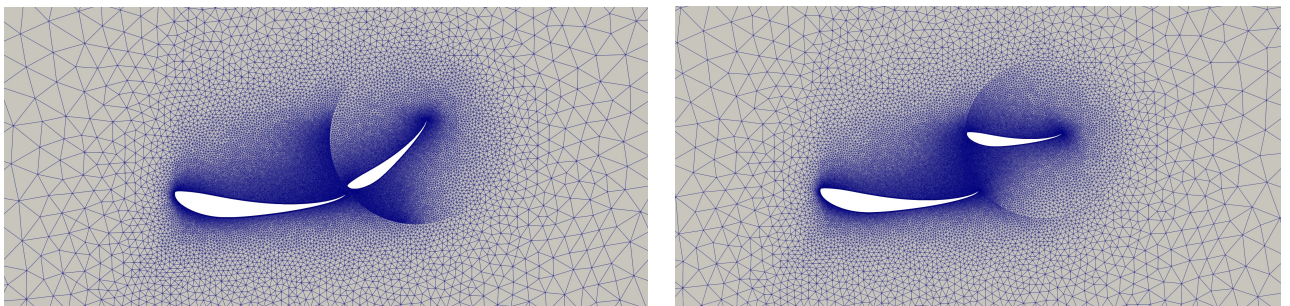


Figure 1: Sliding mesh for the disabled (left) and enabled (right) DRS

Both airfoils are surrounded by a structured boundary layer (BL) mesh, that extends for a thickness of 0.01 with a growing ratio of 1.0922. The thickness of the first cell was adjusted to fulfill, along the airfoil contour, the requirement of  $y^+ \leq 1$ , needed to properly solve the velocity profile of the boundary layer when, as in this case, wall functions are not employed. This translates into a thickness of  $h_0 = 2 \cdot 10^{-6}$  for the DRS wing, while for the mainplane, after observing higher values of  $y^+$  close to the leading edge, this value was reduced to  $h_0 = 1.3 \cdot 10^{-6}$ .

The remaining part of the mesh is made up of an unstructured triangular mesh, generated by the Delaunay algorithm. The local size of the elements varies within the domain, from the smaller cells around the structured mesh of the BL to the largest cells at the far field, with a prescribed size of  $h = 2$ . One of the most important aspects of the mesh generation in a sliding mesh approach is the size of the elements along the interface between the two zones in relative motion. A small size of the elements is desirable in this region to allow for better interpolation of the flow features between the cells of the two subdomains. To balance the need for small cells and that of keeping the global number of cells within a range compatible with the available computational power, a size of  $h = 2.8 \cdot 10^{-2}$  has been selected for most of the interface.

The portion of the circumference closer to the trailing edge of the mainplane and the leading edge of the DRS has been further refined to a size comparable to that of the cells at the BL edge. Since the gap between the airfoils is tight, the edge of the BL ends up being very close to the interface. To avoid generating excessively skewed cells, the size of the elements in this portion of the interface is set to  $h = 2.1 \cdot 10^{-3}$ . This refined portion covers an arc of 48°, which is shifted between the two zones to ensure that the trailing edge of the mainplane and the leading edge of the DRS remain close to similar-sized cells throughout the entire motion. Inevitably, during the rotation, along the interface, larger cells from one zone will be next to smaller ones in the other. This happens only in limited regions, further from the airfoils, and it is not affecting in a relevant way residuals and convergence. Imposing a very fine cell size all over the interface would improve the mesh but excessively increase the number of points, thus it has been discarded.

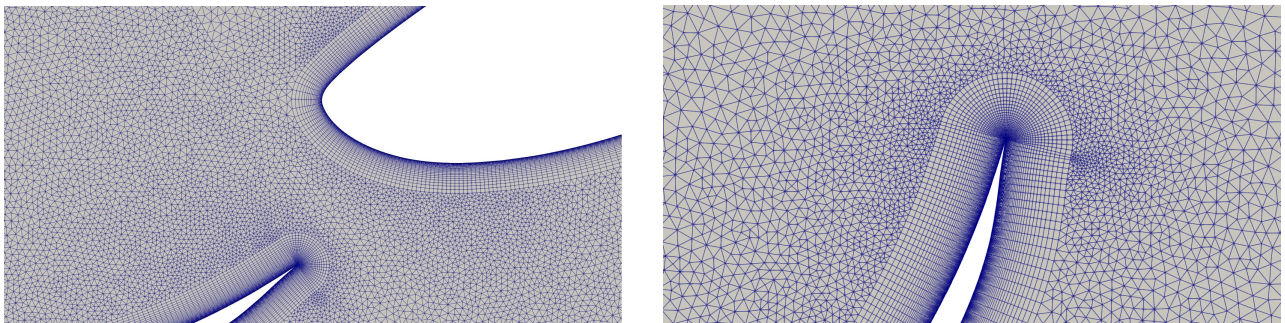


Figure 2: Boundary layer meshes at the interface (left) and at the trailing edge of the DRS (right)

### 2.2.1 Gurney flap

Generating the mesh for the DRS wing equipped with the Gurney flap has brought additional challenges. While the mainplane mesh has been recovered from the previous geometry, the zone pertaining to the DRS wing has been completely revised.

The automatic BL meshing tool provided by GMSH is not capable of dealing with sharp convex corners, such as the one formed by the pressure side of the DRS wing and the upstream side of the Gurney flap. As a workaround, the BL is meshed by resorting to transfinite surfaces.

A MatLab routine extracts a refined airfoil contour, retrieved from a spline interpolation of the original contour points. A rectangle is attached to the trailing edge of the DRS wing to model the Gurney flap. The contour is inflated to shape the edge of the BL at a prescribed distance of 0.01 normally to the wall. Concave corners are rendered as rounded corners on the BL edge. To help GMSH correctly catch the geometry, the BL mesh is divided into six regions that are meshed independently as transfinite surfaces. They are partitioned by diagonal lines that originate in corners and points where the airfoil

contour shows a strong curvature (leading edge, trailing edge, and Gurney flap corners). In particular, a diagonal line is drawn in correspondence of the convex corner between the Gurney flap and the pressure side to allow the elements to reorient locally in an effective way. This approach is documented in the literature (Iqbal et al. [5]). Inevitably, the mesh is characterized by a higher degree of skewness. The growing ratio of 1.05 and the number of sublayers in the BL mesh are adjusted to achieve a good aspect ratio, while keeping the parameter  $y^+ \leq 1$  at the wall. In a small number of points, close to the leading edge and in the convex corner, this requirement is not strictly fulfilled, but only by a slight amount that is deemed acceptable ( $y^+ \leq 1.4$ ).

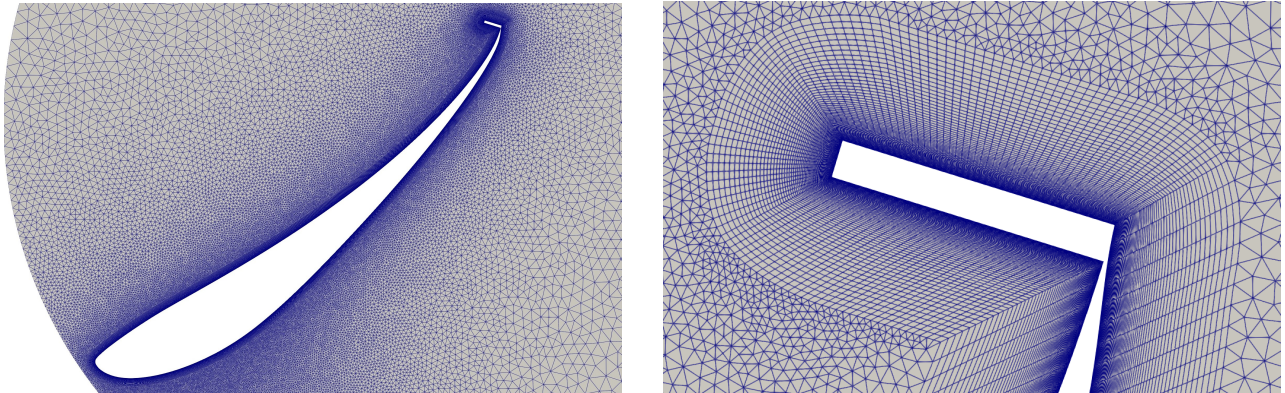


Figure 3: Mesh of the DRS with the Gurney flap (left) and detail of the Gurney flap (right)

## 2.3. Numerical methods

### 2.3.1 Governing equations

The speed of an F1 car at the beginning of a straight, where the DRS is usually activated, is around 200 km/h, close to the maximum speed allowed in the wind tunnel tests carried out by the teams (50 m/s). For air at  $T = 15^\circ\text{C}$ , this corresponds to a Mach number of  $M = 0.15$  and a Reynolds number of  $Re = 3.49 \cdot 10^6$ .

In regions of high curvature of the airfoil contours, the flow is expected to experience a strong acceleration that can lead to velocities twice as high as the free-stream value. Here, Mach numbers that exceed 0.3 may be reached [8]. To account for compressibility effects, the compressible form of the RANS equations has been employed.

### 2.3.2 Convective scheme

The convective scheme used is the approximate *Roe* Riemann solver, an upwind scheme. It is coupled with a MUSCL reconstruction to attain second-order in space. Upwind schemes tend to perform better at high Reynolds numbers, and they are less subject to spurious numerical oscillations. AUSM family schemes have also been evaluated, but they are not compatible with unsteady simulations of moving grids on the SU2 solver.

The *Venkatakrishnan* slope limiter has been set, tuning the coefficient by repeating a number of tests. A value of 0.007 has shown an improved convergence while reducing oscillations during iterations of the steady simulation.

The turbulent convective scheme is a *scalar upwind* scheme without MUSCL reconstruction.

Gradient calculation is performed by the *Weighted Least Squares* method. The *Green-Gauss* method led to divergence at the interface between the two zones.

### 2.3.3 Turbulence model

An appropriate turbulence model should be selected for the closure of the RANS equations. Two models have been taken into account: Spalart-Allmaras (SA) and  $k-\omega$  SST.

The SA model is a one-equation model; it is computationally cheap but has trouble in flows with system rotation and does not always work with separated regions. The latter limitation is significant because, due to the adaptations to the geometry required for the sliding-mesh approach, it is not guaranteed that the DRS will work as intended and significant separated regions could appear.

The SST model, on the other hand, is a two-equation model, more computationally expensive but better suited close to walls and in the far field regions. Thereby, and in agreement with the literature [7], the SST model has been selected.

### 2.3.4 Boundary and freestream conditions

The following conditions are imposed:

- freestream Mach number  $M = 0.15$ ;
- freestream pressure  $p = 101325 \text{ Pa}$ ;
- freestream static temperature  $T = 288.15 \text{ K}$ ;
- angle of the incoming flow  $\alpha = -4^\circ$ .

The incoming flow is not horizontal to retain a more realistic angle of attack for the rear wing, which also accounts for the downward deflection of the flow due to the presence of the engine hood.

Concerning wall boundary conditions, to impose a no-slip condition on an adiabatic wall, the marker *heatflux* is set to zero, both for the mainplane and the DRS.

The use of *sliding meshes* requires a special treatment of the boundary conditions of the interface between the zones. For this reason, the marker *fluid interface* and the marker *zone interface* have been set to enable information exchange. Furthermore, to interpolate the solution, the *weighted average* method has been preferred, taking into account that throughout the motion cells are misaligned and communication must be ensured between more than two adjacent cells.

### 2.3.5 Convergence criteria

The strategy to control that convergence is met provides for checking both Cauchy convergence of the aerodynamic coefficients and residuals. Cauchy convergence ensures that the oscillations of the aerodynamic coefficients are limited, a critical aspect to be able to study how transient phenomena or alternative configurations (e.g., the Gurney flap) impact on the performance of the rear wing. Residuals are monitored so that the solution in the broader flow field is well developed, especially in the presence of turbulent phenomena.

For Cauchy convergence, values below  $10^{-5}$  over 100 elements have been prescribed for the lift and drag coefficients of both the mainplane and the DRS airfoils.

In unsteady simulations, the RMS of the residuals of the energy equation is monitored together with the maximum residuals of turbulent kinetic energy, and both are required to be below  $10^{-5}$ . A condition on the energy equation has been implemented because it was not converging effectively within each time step in the region close to the interface.

In steady simulations, performed for the grid independence analysis and the Gurney flap configuration, stricter criteria have been imposed on the maximum residuals of turbulent kinetic energy, which have been required to be below  $10^{-7}$ , as this is instrumental to achieve a good solution in the region immediately downstream of the movable wing of the DRS.

### 2.3.6 Unsteady simulation

The time window for the opening of the DRS lasts  $\Delta t = 0.2 \text{ s}$ , during which the airfoil transitions from an initial angle of  $-40^\circ$  relative to the horizontal to being completely horizontal (at  $0^\circ$ ). Since the total angle swept by the DRS is  $\Delta\alpha = 40^\circ$ , it follows that the required angular velocity to impose on the moving flap is  $\omega = \Delta\alpha/\Delta t = 3.49 \text{ rad/s}$ .

The SU2 solver only accepts sinusoidal oscillations and motions with constant velocity. To perform the simulation as desired, it has been divided into three distinct phases:

1. DRS disabled (0 to 0.4 s): this phase corresponds to a closed DRS flap;
2. Activation (0.4 to 0.6 s): the opening of the DRS is simulated as a rigid motion starting and ending impulsively;
3. DRS enabled (0.6 to 1.2 s): in this final phase, the DRS flap is open.

The solver advances to the subsequent phase by taking as the restart solution the last time step of the previous one to guarantee numerical consistency. A reliable solution is required at the end of each phase, as it will feed the next one.

Among the available temporal schemes (*time-stepping*, *dual time-stepping first-order*, and *dual time-stepping second-order*), the second-order scheme diverged. First-order methods introduce greater numerical damping that reduces instabilities, at the cost of a larger truncation error. Thus, the temporal scheme used is the *dual time-stepping first-order*, with an *Euler implicit* time discretization.

The time step for the unsteady simulation is  $\Delta t = 8 \cdot 10^{-4} s$ . This implies that the Courant-Friedrichs-Lowy number computed on the smallest element at the interface is  $CFL = 58.8$ . A time convergence analysis has been performed to ensure temporal independence, as reported in Section 3.1.

### 3. Verification and validation

#### 3.1. Verification

**Domain independence** The radius of the far field was selected by carrying out a domain independence analysis. Three simulations have been performed for different radii (20, 40 and 80 chords), as shown in Figure 4, and the results have been analyzed in terms of the percentage change of the aerodynamic coefficients, both for the mainplane and for the DRS.

Two aerodynamic coefficients show variations of less than 1%, the DRS lift coefficient is slightly higher (1.09%) and the greatest variation (mainplane drag) is still less than 2%. These variations are considered acceptable also considering time saving, which is extremely important in case of unsteady simulations, hence the value  $R = 40$  has been selected as far-field radius.

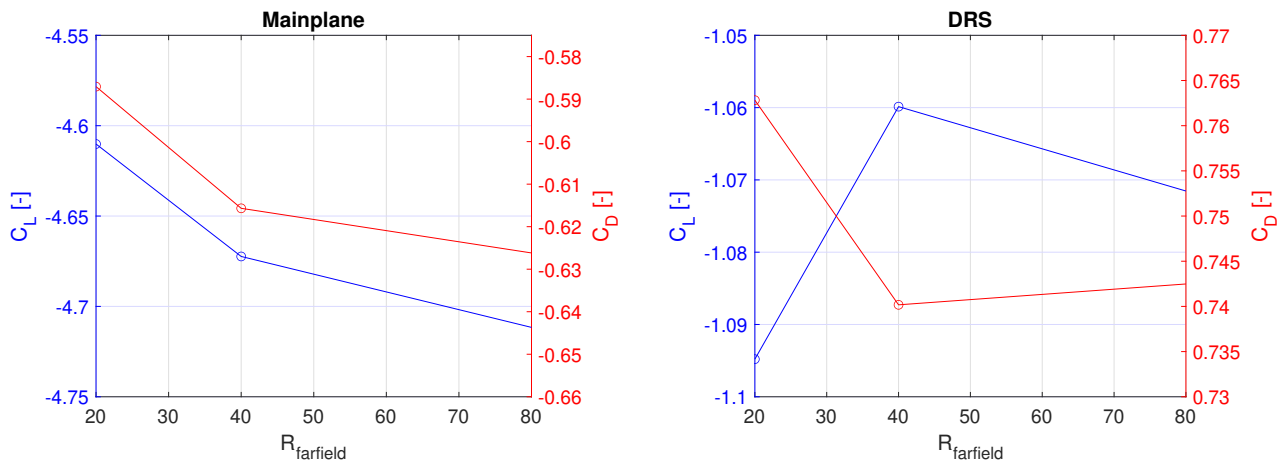


Figure 4: Aerodynamic coefficients (lift in blue and drag in red), both for mainplane and DRS, for different far-field radii

Radii	Mainplane		DRS	
	$\Delta C_L$	$\Delta C_D$	$\Delta C_L$	$\Delta C_D$
20-40	1.33%	4.65%	3.30%	3.06%
40-80	0.83%	1.68%	1.09%	0.31%

Table 1: Percentage change of the aerodynamic coefficients during the domain convergence analysis

**Grid independence** To verify the independence of the results from grid refinement, the starting grid has been refined and coarsened by a factor  $f = \sqrt{2}$ , to approximately double and halve the number of cells. For the disabled DRS configuration, steady simulations have been performed on each mesh to check that the change of the aerodynamic coefficients from grid to grid is below an acceptance tolerance.

Mesh	Number of cells			Growth rate		Venkat coefficient
	Total	Mainplane	DRS	Mainplane	DRS	
Coarse	93540	62577	30963	1.1412	1.2239	0.010
Medium	184532	123179	61353	1.0922	1.1447	0.007
Fine	360129	238614	121515	1.0603	1.0940	0.005

Table 2: Features of the mesh employed in the grid-convergence analysis

To refine the boundary layer, modifying neither the global thickness nor that of the first cell, the growth ratio of the BL is altered to maintain the aspect ratio of its cells. The size of the cells in the direction tangential to the wall is directly affected by the refinement factor. To preserve the aspect ratio, on average, the size in the direction normal to the wall must change by the same quantity. This is obtained by increasing or decreasing the number of sublayers in the BL mesh by a factor  $1/f$ . Given a number of cells in the direction normal to the wall, the size of the first element, and the thickness of the BL, the growing ratio can be determined by means of an analytical formula that has been implemented in a Python routine. As expected, taking this correction into account, the number of elements in the BL mesh changes roughly by a factor  $f^2$  and the aspect ratio of the cells, especially those closer to the edge of the BL, visually improves.

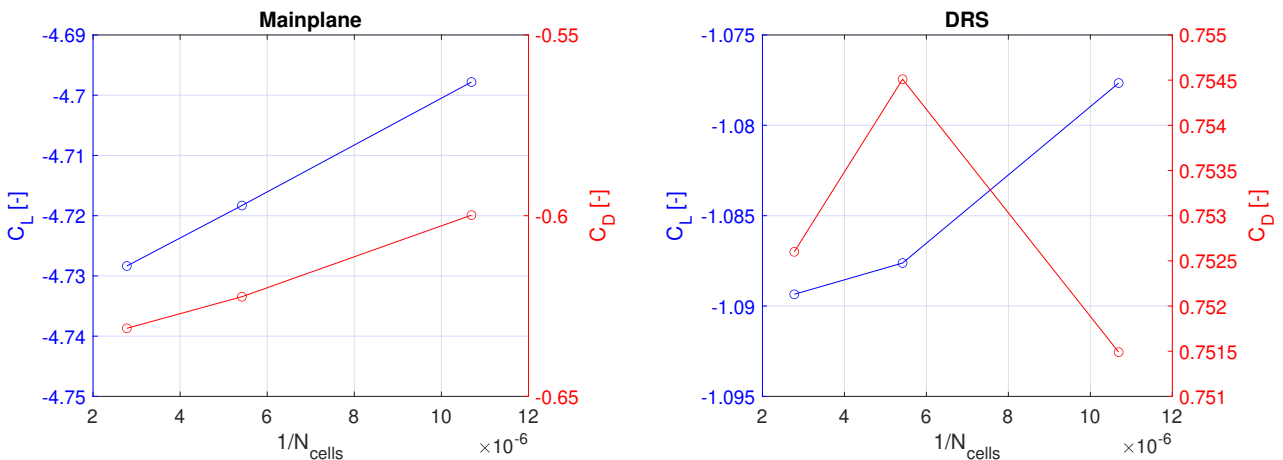


Figure 5: Aerodynamic coefficients (lift in blue and drag in red), both for mainplane and DRS, with different mesh refinements

The number of cells and the growth rate of the BL mesh are synthesized for each mesh in Table 2, together with the Venkatakrishnan coefficient, which has been adapted for the meshes, as suggested

Variation	Mainplane		DRS	
	$\Delta C_L$	$\Delta C_D$	$\Delta C_L$	$\Delta C_D$
Coarse-Medium	0.43%	3.63%	0.92%	0.40%
Medium-Fine	0.21%	1.38%	0.16%	0.25%

Table 3: Percent variations of the aerodynamic coefficients during the grid convergence analysis

in the SU2 documentation [4]. The results of the grid independence analysis can be found in Figure 5 and Table 3.

Three out of four coefficients are below the conventional threshold of 1%; the fourth, although above, has a variation lower than 1.5%. In light of these results, the *Medium* grid has been selected.

**Time independence** A time independence analysis has been conducted for the DRS activation phase to ensure that the time discretization produces reliable results. For this purpose, three simulations have been carried out with different values of  $\Delta t$  and the corresponding CFL numbers, as shown in Table 4.

The error between each time discretization, reported in Figure 6, decreases as the size of the time step decreases and falls below 1% when transitioning from the medium time step to the fine one, which is acceptable.

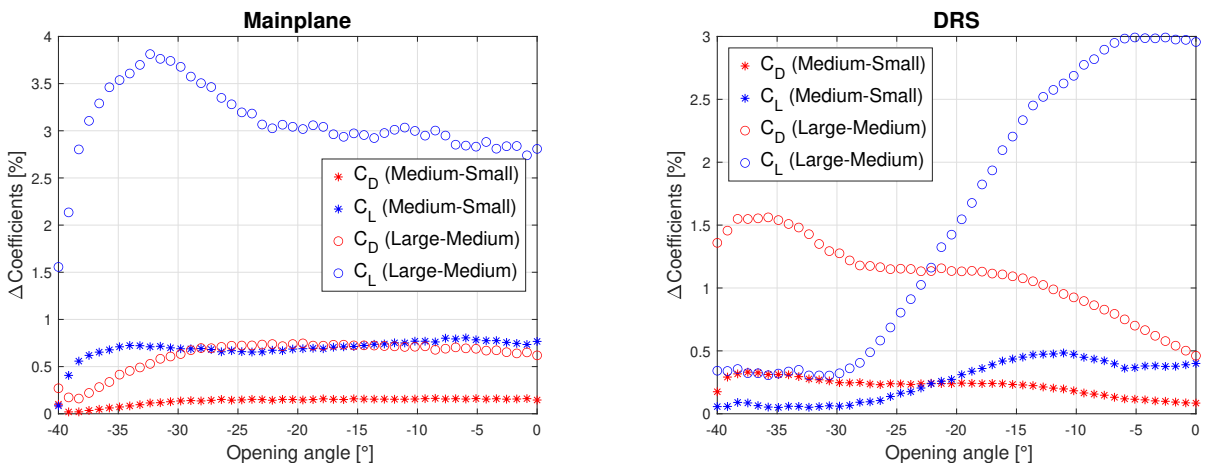


Figure 6: Variations of the aerodynamic coefficients (lift in blue and drag in red), both for mainplane and DRS, with different time refinements through the opening phase

	Small	Medium	Large
$\Delta t$	$1.60 \cdot 10^{-4} \text{ s}$	$8.00 \cdot 10^{-4} \text{ s}$	$4.00 \cdot 10^{-3} \text{ s}$
CFL	11.8	58.8	294

Table 4: Time-steps and CFL numbers for the different refinements employed in the time convergence analysis

### 3.2. Validation

To seek validation of the methodology applied in this paper and the model employed for the CFD simulations performed, available studies in the literature, including Dimastrogiovanni et al. [3], Ahsan [1] and Louçao et al. [7], have been taken as benchmarks for the work conducted in this report. These

sources provide limited information on experimental data or unsteady simulations, but offer figures for steady simulations on similar geometries.

A comparison between the aerodynamic loads retained from a set of steady simulations at different opening angles of the DRS flap and data from Dimastrogiovanni et al. and Ahsan is reported in Figure 7.

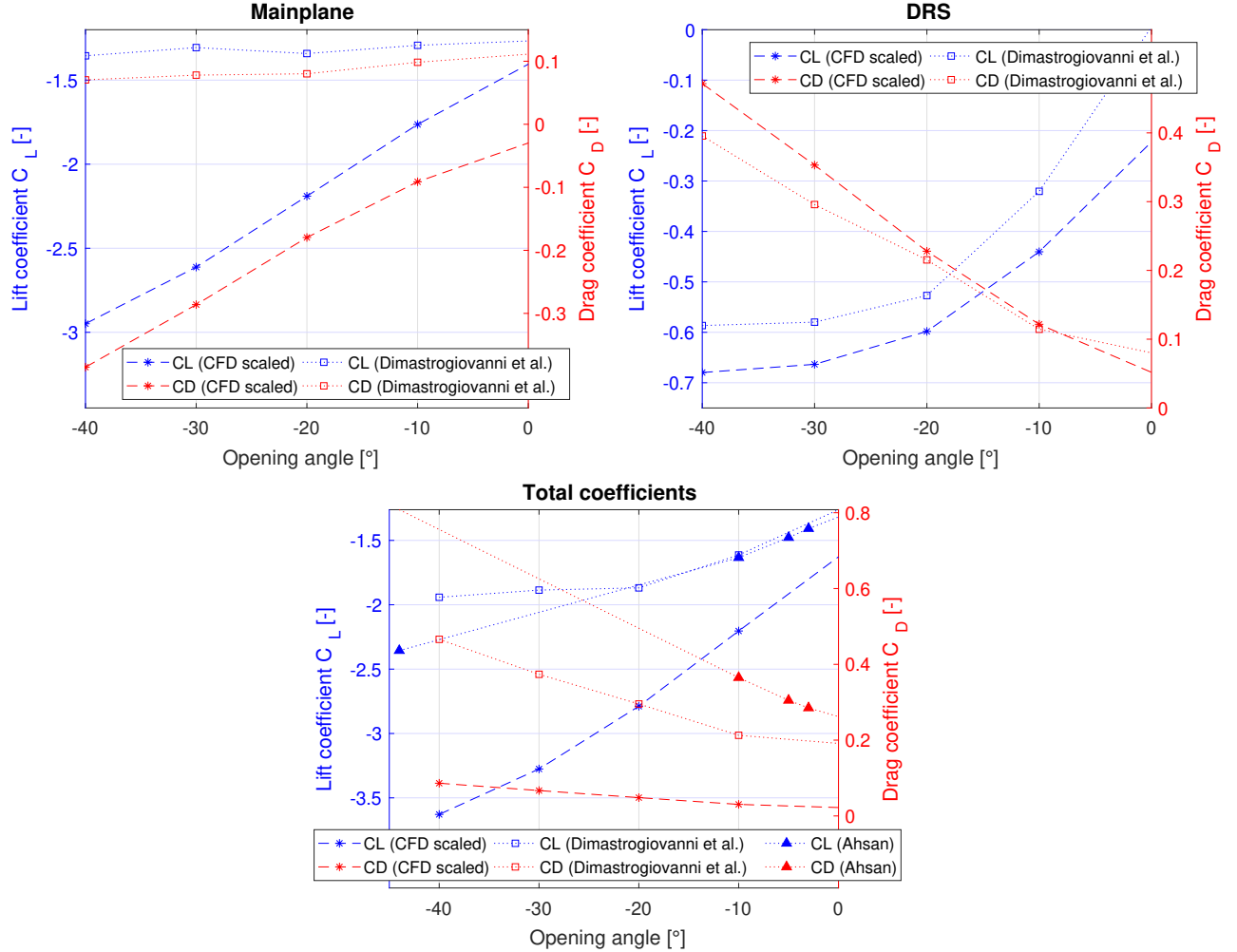


Figure 7: Comparison of aerodynamic coefficients at different opening angles of the DRS with the literature (Dimastrogiovanni et al. [3], Ahsan [1])

Both studies have implemented full 3D models of the rear wing and are able to catch flow features that are expected to affect the results obtained. A 2D analysis is a very limited approach for modelling the rear wing of a racing car, that is affected by the aerodynamics of the body of the car, 3D velocity and vorticity fields, short span wings, presence of ground and a number of other effects.

The geometries found in the literature could not be fully replicated due to the constraints imposed by the sliding mesh approach, as discussed in Section 2.1. Moreover, some details about the models are missing and have been retrieved as approximative values from the available data combined with sketches and plots, as they are needed to estimate the normalizing surface for the computation of the coefficients. The study by Dimastrogiovanni et al. is conducted using NACA 16520 and NACA 13509 airfoils, which perform in a markedly distinct way with respect to the S1223 airfoil. The DRS flap in Ahsan appears to be slightly smaller in proportion by an estimated 10%. Both studies replicate similar free-stream conditions, with inlet velocities of respectively  $50\text{ m/s}$  and  $42\text{ m/s}$ . The aerodynamic coefficients of the CFD simulations have been rescaled using the total chord  $c = c_{ref} + 0.6 \cdot c_{ref} = 1.6$ . Despite the non-rigorous data collection and the limitations mentioned above, qualitative considerations can be drawn. The results for the DRS flap show better agreement with the sources, at least

in terms of general trends, both for drag and lift. However, the mainplane deviates significantly from the collected data, and it is affected by the change of the opening angle in a much larger way. The presence of the DRS has more impact on the aerodynamics of the main wing, and this is also reflected in the total coefficients.

A notable difference between the behavior of the model proposed in this paper and the studies cited above is the position of the stagnation point at the leading edge of the main wing. As observed in Section 4.1, the stagnation point is pronouncedly shifted toward the pressure side of the airfoil, as a consequence of the presence of the DRS flap. This circumstance does not appear in the works cited, but is recognized in Louçao et al., which proposes a 2D study of a three-element rear wing, with S1223 airfoils. This suggests that neglecting the 3D effects may be causing the occurrence of unexpected modifications to the flow field.

In light of this review, the results and conclusions that follow should be intended as qualitative analyses aimed at understanding only some aspects of the proposed problem, conducted with the limited tools, computational power, and time available for this work.

## 4. Results

### 4.1. Steady simulation

Steady simulations were carried out for grid convergence and validation purposes. However, a result worth highlighting is the negative value assumed by the mainplane drag. A possible cause for this apparently unphysical result is an issue sometimes encountered in SU2 when dealing with multiple bodies. On the other hand, observing the pressure field represented in Figure 8, it is possible to notice how the low pressure zone generated by the profile, due to its shape, is shifted towards the leading edge. Moreover, the presence of the DRS generates a strong high pressure zone at the back. Combining these two effects, it could be reasonable that looking only at the mainplane, the computed drag is negative provided that, as it happens, the global drag remains positive. As anticipated in Section 3.2, very few data are available for 2D analyses of such configuration and only in terms of global coefficients, so no information on the coefficients of the individual airfoils could be retrieved.

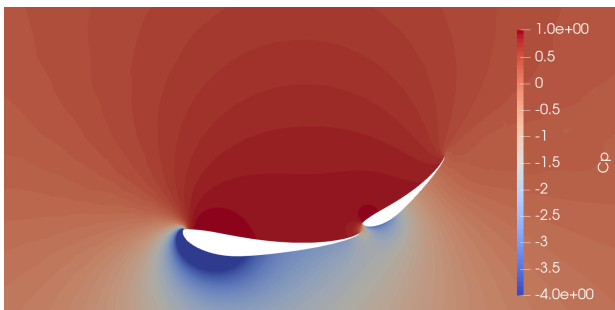


Figure 8: Pressure coefficient around the rear-wing with closed DRS

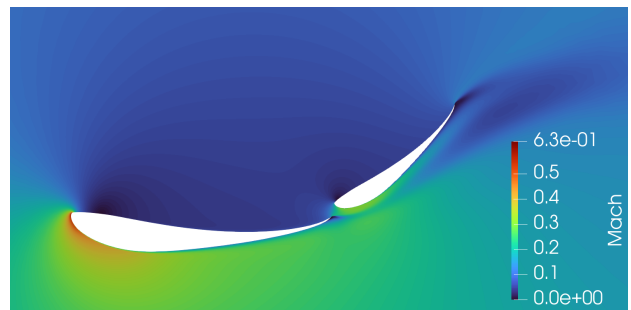


Figure 9: Mach number around the rear-wing with closed DRS

Two other noticeable results can be deduced from the representations of the Mach number in Figure 9 and of the streamlines in Figure 10. Looking at the Mach in the domain, it clearly exceeds the threshold of  $M = 0.3$ , reaching values of 0.6, in regions close to the leading edge of the mainplane and in the small gap between the airfoils. This justifies the choice of the compressible form for the governing equations. Observing the streamlines, it is noted how the stagnation point on the mainplane is shifted along the pressure side and also that, on the back of the DRS, the flow remains attached despite the changes to the geometry of the problem introduced for the use of the sliding mesh. The only separated regions are the small recirculation bubbles that appear at the sharp trailing edge of both airfoils, as highlighted in Figure 11.

The results in terms of aerodynamic coefficients for the two DRS configurations are summarized in Table 5. As expected, when the DRS is open, a significant reduction both in downforce and drag is present with variations with respect to the closed configurations equal to  $\Delta C_L = -55.15\%$  and

$\Delta C_D = -72.93\%$ . These values are probably overestimated as a consequence of the over-evaluation of the coefficients in the closed configuration previously discussed in Section 3.2.

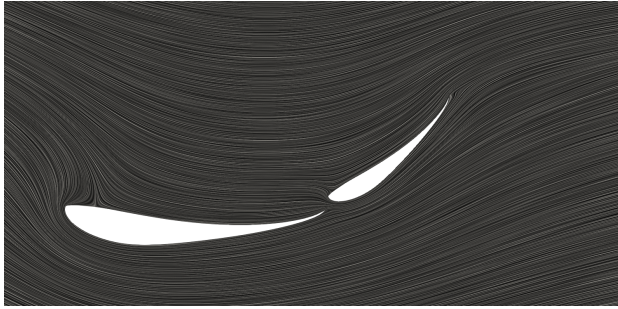


Figure 10: Streamlines around the rear-wing with closed DRS

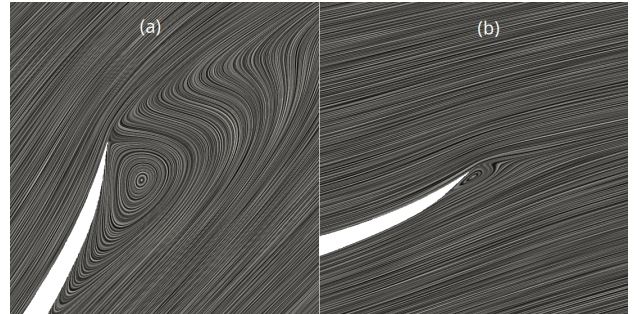


Figure 11: Streamlines at the trailing edge of the DRS for the closed (a) and open (b) flap

Configuration	Mainplane		DRS		Total	
	$C_L$	$C_D$	$C_L$	$C_D$	$C_L$	$C_D$
DRS close	-4.718	-0.622	-1.088	0.755	-5.806	0.133
DRS open	-2.248	-0.047	-0.356	0.083	-2.604	0.036

Table 5: Aerodynamic coefficients computed with steady simulations for both the DRS configurations

## 4.2. Unsteady simulation

Unsteady simulations are crucial to understand how transient phenomena can affect car performance. The simulation has been carried out using the intermediate time step  $\Delta t = 8 \cdot 10^{-4} s$ , with an initial phase of  $0.4 s$ , an opening phase  $0.2 s$  and a final phase with the DRS open of  $0.6 s$ . In Figure 12, it is possible to observe the vorticity field associated with the initial instants, characterized by the formation of the starting vortex. The starting vortex, which has a circulation opposite to that of the airfoils, induces an additional velocity component that reduces the angle of attack (that becomes less negative) and consequently lift. Furthermore, the presence of the downstream vortex is associated with an additional drag component. For this reason, the performance of the airfoils is worse compared to steady-state flow conditions. It is therefore necessary to wait for the vorticity and the associated low pressure region to diffuse and move sufficiently far from the airfoils, and for that purpose an interval of  $0.4 s$  has been deemed reasonable.

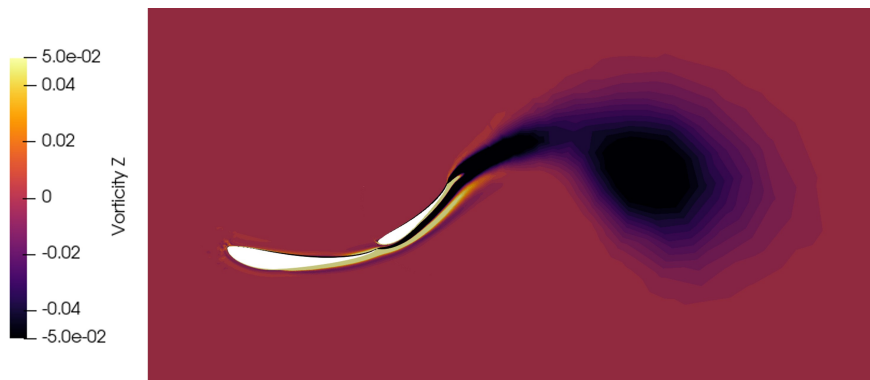


Figure 12: Starting vortex highlighted on the vorticity field ( $z$ -component)

The opening of the DRS flap is a very fast process, in the order of the tenths of a second, but unsteady effects could last longer. The DRS activation zone taken as reference for this work is the first DRS zone

of the Montmeló circuit in Barcelona, which is approximately 400 meters long. At a medium speed of 265 km/h, typical for that portion of the track, this DRS zone is covered in less than 6 seconds. The evolution of the aerodynamic coefficients in time is plotted in Figure 13. A spike is noticed in correspondence of the beginning of the motion of the DRS flap, due to the impulsive start of the actuation. In race cars, the DRS is controlled by a hydraulic system that is not instantaneous due to its characteristic response and inertia. However, the error due to this approximation is expected to be negligible for the aerodynamic performance.

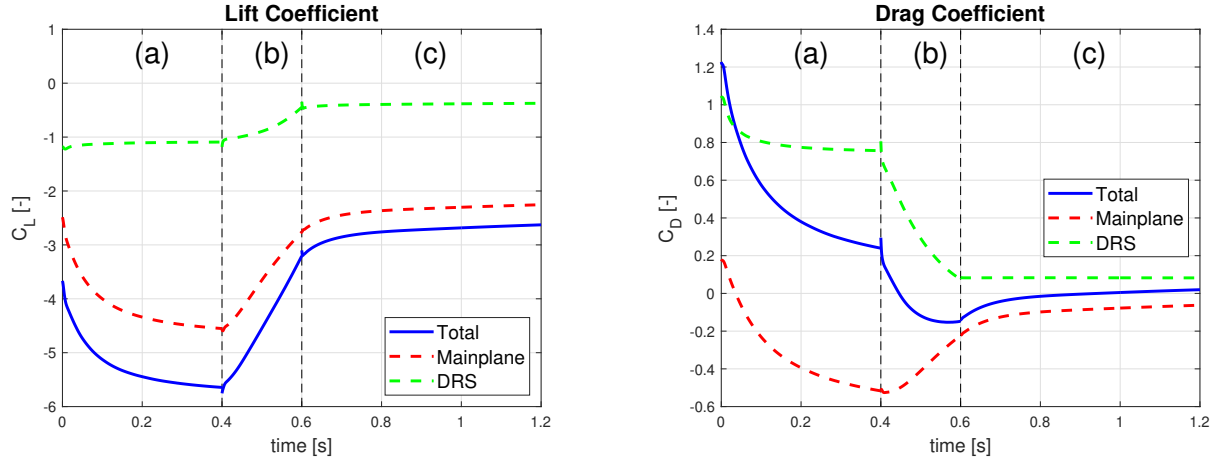


Figure 13: Evolution of the aerodynamic coefficients in time, in phases: (a) DRS disabled, (b) opening phase, (c) DRS enabled

At first, both lift and drag change linearly with the angle of the DRS flap. Interestingly, while the lift coefficient shows linear behavior throughout the entire motion, the drag coefficient becomes more or less stable when the movable surface is about half-open.

When the DRS is fully open the disturbances generated by the motion of the flap continue to be carried by the flow. The loads start converging to the values retained from the steady simulation of the enabled DRS after the motion is completed, and in a time frame that is sufficiently long to be non-negligible with respect to the whole activation of the DRS system.

The aerodynamic coefficients reach steady-state conditions (in the open DRS configuration) in a time in the order of a second after the motion starts, thus transient phenomena affect the performance of the rear wing for 10 to 20% of the total time in which the DRS is enabled on the track.

It is worth highlighting that the lift coefficient at the end of the motion is undershooting its steady-state value, hence remaining more negative initially. This translates into a higher downforce felt by the rear wing, in a moment when the car is accelerating on the straight coming out of the corner. It is a beneficial factor because it allows the tyres to sustain more traction without skidding on the track surface.

At the same time, the drag coefficient is overshooting its steady-state value, up to the point that it is becoming negative overall for a short amount of time. In this transient, the rear wing is giving a positive contribution to the forward motion, pushing the rear wing, and helping the car accelerate.

A vortex can be detected downstream of the rear wing. This vortex is injected into the flow by the changing circulation that results from the opening of the DRS flap. As such, it has a circulation that is opposite, in sign, to that of the starting vortex. When sufficiently close to the rear wing, it induces a velocity component on the airfoils, which has the effect of altering their perceived angle of attack. Due to the influence of the vortex, the mainplane airfoil feels an increased (more negative) angle of attack that contributes to make the lift on the main wing more negative, generating temporarily a larger downforce and a more negative drag. The mainplane perceives larger effects, as it is adapting slower to the changing flow field compared to the DRS flap that is in motion.

As time evolves, the vortex is advected away by the velocity field while diffusing. As this happens, its influence becomes smaller. As a consequence, the induced angle of attack tends to decrease over

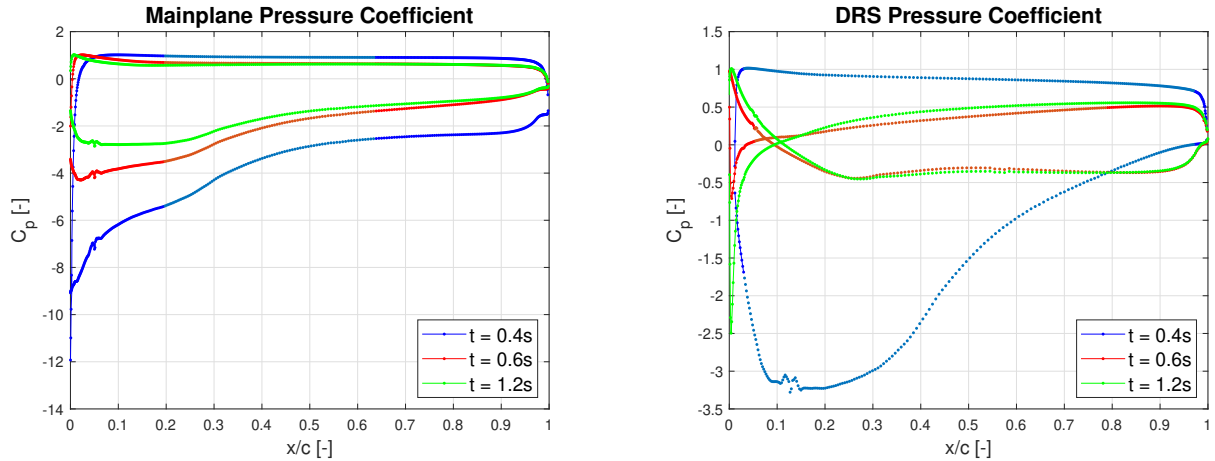


Figure 14: Distribution of the pressure coefficient at the final timestep for each configuration: DRS closed (blue), DRS opened (red) and at the latest timestep (green)

time as the vortex goes away. The peak on the suction side of the mainplane is smeared out as time progresses. The stagnation point travels towards the leading edge of the main wing, while it migrates downstream on the suction side of the DRS flap.

As suggested in Section 3.2, the effects exerted by the presence of the DRS flap on the main wing are likely overestimated by a 2D analysis, therefore it is reasonable to assume that unsteady effects may also be less evident.

The vortex can be traced by looking at the vorticity field at different time steps, as shown in Figure 15. Small recirculation bubbles are recognized at the trailing edge of both airfoils. While that of the main wing is scarcely affected by the evolution of the flow field, the recirculation region behind the DRS flap markedly shrinks down throughout the opening phase, to then stabilize when it comes to a stop.

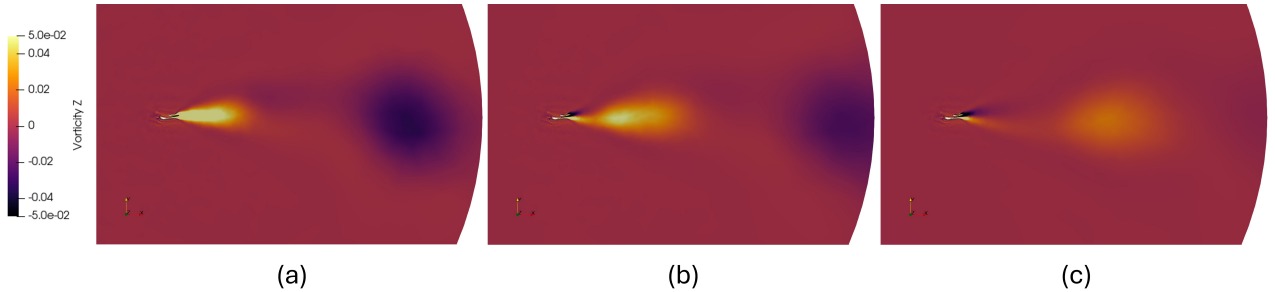


Figure 15: Vortex evolution at different time steps: (a)  $t = 0.6\text{ s}$ ; (b)  $t = 0.72\text{ s}$ ; (c)  $t = 0.92\text{ s}$

### 4.3. Gurney flap

The Gurney flap has been tested for the DRS enabled and DRS disabled geometries, under steady conditions, in its two configurations (0.01 and 0.02 heights). The presence of the Gurney flap mainly changes the pressure distribution on the airfoils. The largest effect is measured close to the trailing edge of the DRS flap, where a peak appears on the pressure side, while increased suction is recorded on the lower surface of the airfoil.

The overall effect is the production of more downforce due to the strong local curvature imposed by the appendage. The distribution of the pressure coefficient on the DRS flap is reported in Figure 16. This behavior is observed when DRS is enabled and disabled, and it appears to be more relevant when DRS is enabled. The taller Gurney flap shows a more notable modification of the pressure distribution. The Gurney flap is a bluff geometry and, as such, induces a large recirculation downstream of it. This

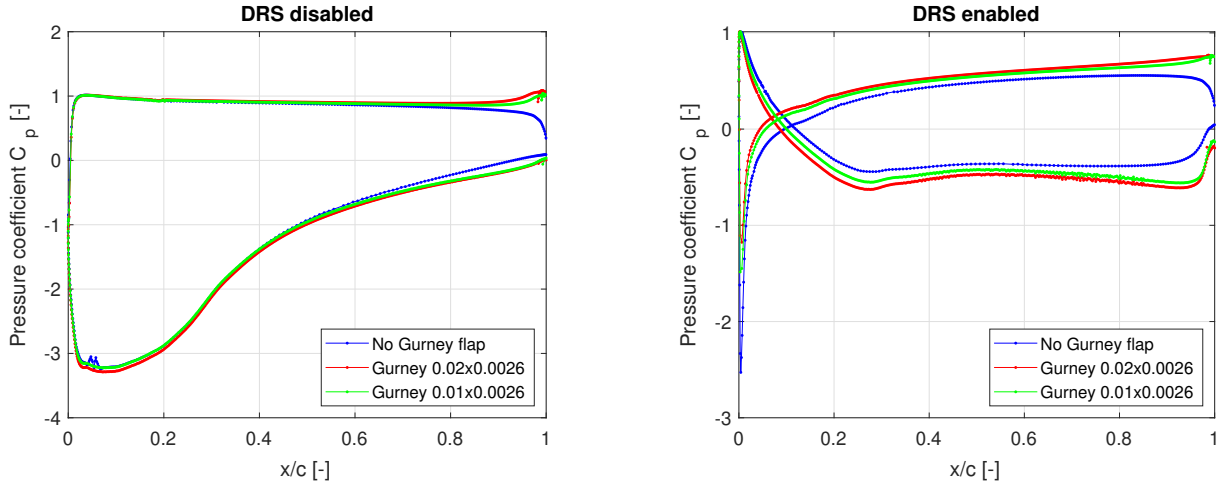


Figure 16: Distribution of the pressure coefficient on the DRS flap, for DRS disabled (left) and DRS enabled (right)

translates into a drag deficit, that may be detrimental for the aerodynamic performance of the wing. For the two configurations, the total lift-to-drag ratio is worse than the case without Gurney flap, with an improvement at smaller heights, as summarized in Table 6. This may or may not be desirable depending on the optimization parameters selected by the strategists and the race engineers for a specific track.

The mainplane is also affected by the presence of the Gurney flap due to the altered behavior of the DRS wing. The suction peak is larger as well and, as a consequence, the airfoil produces more downforce and a more negative drag. However, the drag advantage does not compensate for the drag deficit on the DRS wing.

	DRS disabled			DRS enabled		
	$C_L$	$C_D$	$L/D$	$C_L$	$C_D$	$L/D$
Gurney 0.02x0.0026	-5.937	0.160	37.11	-2.991	0.046	65.02
Gurney 0.01x0.0026	-5.870	0.156	37.63	-2.867	0.041	69.93
No Gurney flap	-5.806	0.133	43.65	-2.604	0.036	72.33

Table 6: Aerodynamic total coefficients and lift-to-drag ratio with and without the Gurney flap

## 5. Conclusions

The present study conducted a comprehensive analysis of the aerodynamic performance of a Formula 1 rear wing equipped with a Drag Reduction System (DRS) and a Gurney flap, employing 2D numerical simulations using the open source CFD software SU2. The investigation, which included both steady and unsteady RANS simulations, yielded insights into the flow dynamics and aerodynamic coefficients characterizing these configurations. The simulations demonstrated the effectiveness of the DRS in reducing aerodynamic drag. Specifically, upon activation, the DRS led to a substantial reduction in the drag and lift coefficients, aligning with the intended functionality of the system to enhance the vehicle's linear speed. The unsteady analysis revealed the starting vortex and the vortex generated in the transient phase during DRS activation. These vortices induced a temporary modification of the effective angle of attack on the aerodynamic surfaces. The transient phenomena upon activation of DRS, while temporally brief, persisted for approximately one second following the initiation of motion, underscoring their significance in the early stages of DRS deployment. This time frame represents 10–20% of the typical duration of a DRS activation zone, highlighting the importance of accounting for such effects in dynamic performance assessments.

The incorporation of a Gurney flap was analysed under steady-state conditions for both open and closed DRS configurations. The results confirmed that the Gurney flap effectively enhanced aerodynamic performance by increasing lift while introducing only a moderate penalty in drag. Among the configurations tested, the shorter Gurney flap (0.01x0.0026) demonstrated a more balanced performance. The taller Gurney flap (0.02x0.0026), while further increasing downforce, produced a lower lift-to-drag ratio, suggesting that its implementation should be carefully evaluated based on specific track requirements and race strategies.

The results provide qualitative and quantitative insights, although the limitations of the 2D modelling approach must be acknowledged. Key 3D aerodynamic phenomena, such as ground effects, spanwise flow variations, vortex shedding, and interactions between the wing and the vehicle body, were excluded. These omissions likely contributed to discrepancies in the computed aerodynamic coefficients, particularly for the mainplane, where the simplified representation of the S1223 airfoil deviates from the complex geometries of real Formula 1 wings. Additionally, constraints imposed by the sliding mesh methodology necessitated geometric simplifications that may have influenced the flow field, particularly in the interaction regions.

Further implementations should prioritize extending the analysis to 3D simulations, which are essential for capturing critical aerodynamic effects that govern the performance of Formula 1 rear wings in realistic conditions. Additionally, exploring the interaction between the DRS and other aerodynamic components, as well as conducting a more detailed analysis of transient effects, could lead to improved designs for both the DRS and the Gurney flap.

## References

- [1] Mahim Ahsan. Numerical study on aerodynamic drag reduction on a rear wing of a Formula student car. Master's thesis, KTH Royal Institute of Technology, 2021.
- [2] Fernanndo M. Catalano and G. L. Brand. Experimental and numerical study of a two-element wing with Gurney flap. In *25TH International Congress of the Aeronautical Sciences (ICAS 2006)*, Hamburg, Germany, September 2006.
- [3] Mauro Dimastrogiovanni, Giulio Reina, and Andrea Burzoni. An improved active drag reduction system for Formula race cars. *Proceedings of the Institution of Mechanical Engineers, Part D: Journal of Automobile Engineering*, 234(5):1460–1471, April 2020.
- [4] SU2 documentation. Slope limiters and shock resolution. [https://su2code.github.io/docs\\_v7/Slope-Limiters-and-Shock-Resolution/](https://su2code.github.io/docs_v7/Slope-Limiters-and-Shock-Resolution/) (visited on January 21, 2025).
- [5] Muhammad Yousaf Iqbal, Syed Irtiza Ali Shah, and Ali Hassan. CFD analysis of NACA-0012 airfoil with various porous Gurney flap geometries. In *2019 International Conference on Applied and Engineering Mathematics (ICAEM)*, pages 231–236, Taxila, Pakistan, 2019. IEEE.
- [6] Cory S. Jang, James C. Ross, and Russell M. Cummings. Numerical investigation of an airfoil with a Gurney flap. *Aircraft Design*, 1(2):75–88, 1998.
- [7] Ricardo Loução, Gonçalo Duarte, and Mário Mendes. Aerodynamic study of a Drag Reduction System and its actuation system for a Formula student competition car. *Fluids*, 7:309, September 2022.
- [8] Federico De Santis. Experimental investigation of a F1 car rear wing equipped with an active drag reduction system. Master's thesis, Politecnico di Milano, December 2024.
- [9] Junwei Yang, Hua Yang, Weijun Zhu, Nailu Li, and Yiping Yuan. Experimental study on aerodynamic characteristics of a Gurney flap on a wind turbine airfoil under high turbulent flow condition. *Applied Sciences*, 10(20):7258, October 2020.